

Cycle Consistent Adversarial Denoising Network for Multiphase Coronary CT Angiography

Eunhee Kang, Hyun Jung Koo, Dong Hyun Yang, Joon Bum Seo, and Jong Chul Ye*, *Senior Member, IEEE*

Abstract—In coronary CT angiography, a series of CT images are taken at different levels of radiation dose during the examination. Although this reduces the total radiation dose, the image quality during the low-dose phases is significantly degraded. To address this problem, here we propose a novel semi-supervised learning technique that can remove the noises of the CT images obtained in the low-dose phases by learning from the CT images in the routine dose phases. Although a supervised learning approach is not possible due to the differences in the underlying heart structure in two phases, the images in the two phases are closely related so that we propose a cycle-consistent adversarial denoising network to learn the non-degenerate mapping between the low and high dose cardiac phases. Experimental results showed that the proposed method effectively reduces the noise in the low-dose CT image while preserving detailed texture and edge information. Moreover, thanks to the cyclic consistency and identity loss, the proposed network does not create any artificial features that are not present in the input images. Visual grading and quality evaluation also confirm that the proposed method provides significant improvement in diagnostic quality.

Index Terms—deep learning, low-dose CT, semi-supervised learning, generative adversarial network (GAN), cyclic loss

I. INTRODUCTION

X-RAY computed tomography (CT) is one of the most widely used imaging modalities for diagnostic purpose. For example, in cardiac coronary CT angiography (CTA), a series of CT images are acquired while examination is conducted with contrast injection [1], which helps clinicians to identify the degree of calcification of coronary artery and stenosis in the coronary artery of the heart.

However, radiation exposure from CT can increase potential cancer risks. To reduce the risk of radiation exposure, in coronary CTA the x-ray tube current is modulated for each cardiac phase as shown in Fig. 1. Although this tube current modulation can reduce the total radiation dose, this results in CT images with different noise levels and contrast at different cardiac phases (see Fig. 1). Specifically, it introduces noises in the projection data of the low-dose phases, which deteriorates the reconstruction image quality. Although model-based iterative reconstruction (MBIR) methods [2]–[8] have been developed to address this, the MBIR approaches suffer from relatively long reconstruction time due to the iterative applications of forward and back projections.

EK and JCY are with the Department of Bio and Brain Engineering, Korea Advanced Institute of Science and Technology (KAIST), Daejeon 34141, Republic of Korea (e-mail: {eunheekang,jong.ye}@kaist.ac.kr). HJK, DHY, and JBS are with Department of Radiology, Asan Medical Center, University of Ulsan College of Medicine, Seoul 05505, Republic of Korea (email: {elfin19,donghyun.yang,joonbeom.seo}@gmail.com).

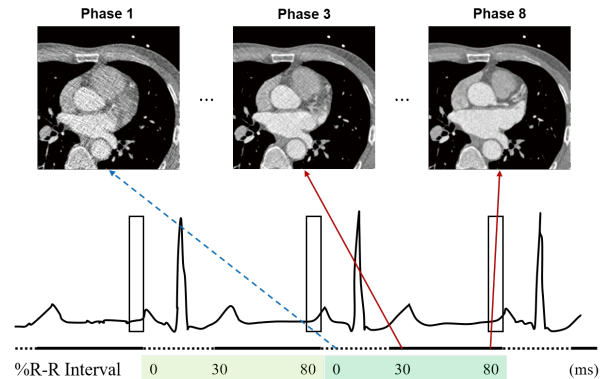


Fig. 1. Example of multiphase coronary CTA acquisition protocol. Low-dose acquisition is performed in phase 1 and 2, whereas routine-dose acquisition is done in phase from 3 to 10.

Recently, deep learning approaches have demonstrated impressive performance improvement over conventional iterative methods for low-dose CT [9]–[12] and sparse-view CT [13]–[16]. The main advantage of deep learning approach over the conventional MBIR approaches is that the network learns the image statistics in a fully data-driven way rather than using hand-tuned regularizations. While these approaches usually take time for training, real-time reconstruction is possible once the network is trained, making the algorithm very practical in the clinical setting.

While these networks have been designed based on supervised learning technique, in real clinical situation matched low- and routine- dose CT image pairs are difficult to obtain, since patients should undergo multiple scans with additional radiation exposure to get paired CT images. To address this unmatched pair problems, Wolterink et al [17] proposed a low-dose CT denoising network with generative adversarial network (GAN) loss so that the distribution of the denoising network outputs can match the routine dose images. However, one of the important limitations of GAN for CT denoising [17]–[19] is that there is a potential risk that the network may generate features that are not present in the images due to the degeneracy of the mapping. This is because GAN network is trained to match the data distributions but it does not guarantee that an input and output data are paired in a meaningful way, i.e. there can exist various inputs (resp. outputs) that matches to one output (resp. input) despite them generating the same distribution.

In coronary CTA, even though the images at the low-dose and high-dose phases do not match each other exactly due to

the cardiac motion, they are from the same cardiac volume so that they have important correspondence. Therefore, one can conjecture that the correctly denoised low-dose phase should follow the routine dose phase image distribution more closely and learning between two phase cardiac images is more effective than learning from totally different images. One of the most important contributions of this work is to show that we can indeed improve the CT images at the low-dose phase by learning the distribution of the images at the high-dose phases using the *cyclic consistency* by Zhu et al. (cycleGAN) [20] or by Kim et al. (DiscoGAN) [21].

More specifically, we train two networks, $G_{AB} : A \rightarrow B$ and $G_{BA} : B \rightarrow A$, where A and B are two different domains (low dose and routine dose), and G_{AB} is the network with A domain as input and B as output. Similarly, the network G_{BA} is defined. Then, the training goal is that G_{AB} and G_{BA} should be inverse of each other, i.e. $G_{BA}(G_{AB}(x_A)) \approx x_A$ and $G_{AB}(G_{BA}(x_B)) \approx x_B$. Thanks to the existence of inverse path, the degeneracy problem of the GAN network described above can be avoided. Another important contribution of this paper is the introduction of the identity loss [20]. In contrast to the standard cycle GAN [20], the changes that we expect from the generator are only the noise contributions that should be considered to avoid generating artificial features that are not present in the input images. Experimental results show that the proposed method is robust to the cardiac motion and contrast changes from contrast agent injection.

II. METHOD

A. Overall Framework

The overall framework of the proposed network architecture is illustrated in Fig. 2. We denote the low-dose CT domain by (A) and routine-dose CT domain by (B), and the data distribution for each domain is referred to as P_A and P_B , respectively. The generator G_{AB} denotes the mapping from (A) to (B), and G_{BA} are similarly defined as the mapping between (B) to (A). As for the generator, we employ the optimized network for a noise reduction in low-dose CT images in [10]. In addition, there are two adversarial discriminators D_A and D_B which distinguish between measured input images and synthesized images from the generators. Then, we train the generators and discriminators simultaneously. Specifically, we aim to solve the following optimization problem:

$$\min_{G_{AB}, G_{BA}} \max_{D_A, D_B} \mathcal{L}(G_{AB}, G_{BA}, D_A, D_B). \quad (1)$$

where the overall loss is defined by:

$$\begin{aligned} \mathcal{L}(G_{AB}, G_{BA}, D_A, D_B) = & \mathcal{L}_{GAN}(G_{AB}, D_B, A, B) \\ & + \mathcal{L}_{GAN}(G_{BA}, D_A, B, A) \\ & + \lambda \mathcal{L}_{cyclic}(G_{AB}, G_{BA}) \\ & + \gamma \mathcal{L}_{identity}(G_{AB}, G_{BA}), \end{aligned} \quad (2)$$

where λ and γ control the importance of the losses, and \mathcal{L}_{GAN} , \mathcal{L}_{cyclic} and $\mathcal{L}_{identity}$ denote the adversarial loss, cyclic loss, and identity loss. More detailed description of each loss follows.

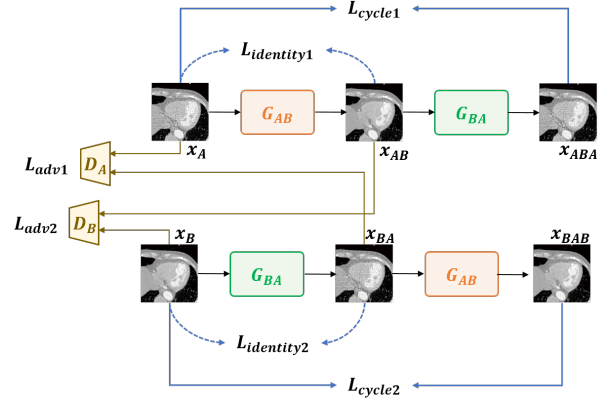


Fig. 2. Overview of the proposed framework for low-dose CT image denoising. There are two generator networks G_{AB} and G_{BA} and two discriminator networks D_A and D_B . A denotes the low-dose CT image domain and B denotes the routine-dose CT image domain. The network employs three losses such as adversarial loss (adv), cyclic loss, and identity loss.

B. Loss formulation

1) *Adversarial loss*: We employ adversarial losses using GAN as proposed in [20]. According to the original GAN [22], the generator (G_{AB}) and discriminator D_B can be trained by solving the following min-max problem:

$$\begin{aligned} \min_{G_{AB}} \max_{D_B} \mathcal{L}_{GAN}(G_{AB}, D_B, A, B) = & \mathbb{E}_{x_B \sim P_B} [\log D_B(x_B)] \\ & + \mathbb{E}_{x_A \sim P_A} [\log(1 - D_B(G_{AB}(x_A)))] \end{aligned} \quad (3)$$

where G_{AB} is trained to reduce a noise in the low-dose CT image x_A to make it similar to the routine-dose CT image x_B , while D_B is trained to discriminate between the denoised CT image $G_{AB}(x_A)$ and the routine-dose CT image x_B . However, we found that the original adversarial loss (3) is unstable during training process; thus, we changed the log-likelihood function to a least square loss as in the least squares GAN (LSGAN) [23]. Then, the min-max problem can be changed to the two minimization problems as follows:

$$\begin{aligned} \min_{G_{AB}} \mathbb{E}_{x_A \sim P_A} [(D_B(G_{AB}(x_A)) - 1)^2], \\ \min_{D_B} \mathbb{E}_{x_B \sim P_B} [(D_B(x_B) - 1)^2] + \mathbb{E}_{x_A \sim P_A} [D_B(G_{AB}(x_A))^2]. \end{aligned} \quad (4)$$

The adversarial loss causes the generator to generate the denoised images that may deceive the discriminator to classify them as the real images at routine doses. At the same time, the adversarial loss will guide the discriminator to well distinguish the denoised image and the routine dose image. Similar adversarial loss is added to the generator G_{BA} , which generates noisy images.

2) *Cyclic loss*: With the adversarial losses, we could train the generator G_{AB} and G_{BA} to produce the realistic denoised images and noisy CT images, respectively; but this does not guarantee that they have an inverse relation described in Fig. 2. To enable one to one correspondence between the noisy and denoised image and to prevent from the degeneracy, the cycle which consists of two generators should be imposed to

bring the input x_A to the original image. More specifically, the cyclic loss is defined by

$$\mathcal{L}_{cyclic}(G_{AB}, G_{BA}) = \mathbb{E}_{x_A \sim P_A} [\|G_{BA}(G_{AB}(x_A)) - x_A\|_1] + \mathbb{E}_{x_B \sim P_B} [\|G_{AB}(G_{BA}(x_B)) - x_B\|_1], \quad (5)$$

where $\|\cdot\|_1$ denotes the l_1 -norm.

3) *Identity loss*: Unlike the style transfer applications as in Zhu et al [20], the domain A and B in our application are low-dose and routine-dose images at different cardiac phases, so they are not drastically different. In fact, once a routine dose image is generated from low dose images (or vice versa), the difference between the input and the output of the networks should be only composed of noises. Therefore, it is reasonable to expect the following conditions:

$$\|G_{AB}(x_A) - x_A\|_1 \leq \epsilon, \quad \|G_{BA}(x_B) - x_B\|_1 \leq \epsilon \quad (6)$$

where ϵ denotes the noise level. To enforce the generators G_{AB} and G_{BA} to satisfy these conditions, we use the identity loss as follows:

$$\mathcal{L}_{identity}(G_{AB}, G_{BA}) = \mathbb{E}_{x_A \sim P_A} [\|G_{AB}(x_A) - x_A\|_1] + \mathbb{E}_{x_B \sim P_B} [\|G_{BA}(x_B) - x_B\|_1]. \quad (7)$$

Similar identity loss was used for photo generation from paintings [20] to preserve color composition between input and output.

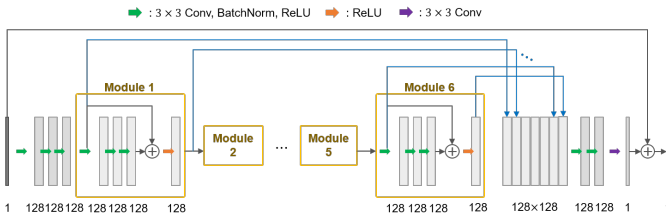


Fig. 3. A generator architecture optimized for the low-dose CT image denoising [10].

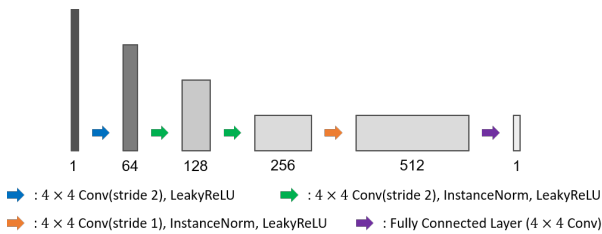


Fig. 4. A network architecture of discriminator [24].

C. Network architecture

The network architecture of two generators G_{AB} and G_{BA} is illustrated in Fig. 3. This architecture is optimized for low-dose CT image denoising in [10]. The first convolution layer uses 128 set of 3×3 convolution kernels to produce 128 channel feature maps. We have 6 set of module composed of 3 sets of convolution, batch normalization, and ReLU layers,

and one bypass connection with a ReLU layer. Convolution layers in the modules use 128 set of $3 \times 3 \times 128$ convolution kernels. In addition, the proposed network has a concatenation layer that concatenates the inputs of each module and the output of the last module, which is followed by the convolution layer with 128 set of $3 \times 3 \times 896$ convolution kernels. This concatenation layer has a signal boosting effect using multiple signal representation [10] and provides various paths for gradient backpropagation. The last convolution layer uses 15 sets of $3 \times 3 \times 128$ convolution kernels. Finally, we add a end-to-end bypass connection to estimate the noise-free image while exploiting the advantages of bypass connection in [25].

The network architecture of discriminators D_A and D_B is illustrated in Fig. 4. This is from PatchGAN [24], which classifies 70×70 overlapping image patches to see whether they are real or synthesized. Specifically, it consists of 5 convolution layers including the last fully-connected layer. The first convolution layer uses 64 sets of 4×4 convolution kernels, and the number of convolution kernels in the following layers is twice that of the previous layer except the last fully connected layer. Arbitrary sized images can be applied to this discriminator network.

III. METHODS

A. Data: Cardiac CT scans

The study cohort comprised 50 CT scans of mitral valve prolapse patients and 50 CT scans of coronary artery disease patients, and the CT scan protocols are described in previous reports [26], [27]. The mean age of the population was 58 ± 13.2 years, and the mean body weight was 66.2 ± 12.6 kg. Using a second generation dual source CT scanner (Somatom Definition Flash, Siemens, Erlangen, Germany), electrocardiography (ECG)-gated cardiac CT scanning was performed. Retrospective ECG-gated spiral scan with ECG-based tube current modulation was applied to multiphase of 0-90% of the R-R interval which comprises with a full dose pulsing window of 30-80% of the R-R interval. The tube current was reduced to 20% of the maximum outside the ECG pulsing window [28] (Fig. 1). A bolus of 70-90 mL of contrast material (Iomeprol, Iomeron 400; Bracco, Milan, Italy) was administered by a power injector (Stellant D; Medrad, Indianola, PA, USA) at a rate of 4.0 mL/s and followed by 40 mL saline. The bolus tracking method (region of interest, the ascending aorta; attenuation threshold level, 100 HU; scan delay, 8 s) was applied to determine scan time. In all CT scans, tube voltage and the tube current–exposure time product were adjusted according to the patients body size, and the scan parameters were as follows: tube voltage, 80-120 kV; tube current–exposure time product, 185-380 mAs; collimation, 128×0.6 mm; and gantry rotation time, 280 s. Mean effective radiation dose of CCTA was 11.4 ± 6.2 mSv. Standard cardiac filter (B26f) was used for imaging reconstruction.

B. Training details

Training was performed by minimizing the loss function (2) with $\lambda = 10$ and $\gamma = 5$. We applied ADAM optimization method to train all networks with $\beta_1 = 0.5$ and $\beta_2 = 0.999$.

TABLE I

STRUCTURES SELECTED AS DIAGNOSTIC REQUIREMENTS TO ASSESS THE DIAGNOSTIC QUALITY OF CARDIAC IMAGES. THE STRUCTURES WERE EVALUATED TO BE SHARP WITH CLEAR VISUALIZATION. (LCA, LEFT CORONARY ARTERY; LV, LEFT VENTRICLE; RCA, RIGHT CORONARY ARTERY; RV, RIGHT VENTRICLE)

Organ	Structure
Left/right coronary artery	LCA ostium
	LCA distal 1.5 cm
	LCA distal
	RCA ostium
	RCA 1.5 cm
	RCA distal
Cardiac wall	LV septum
	RV free wall margin
Cardiac cavity	LV trabeculation
	Left arterial appendage
Aorta	Aortic root
Valve	Aortic valve
	Mitral valve

The number of epochs was 200, which was divided into two phases to control the learning rate during the training. In the first 100 epochs, we set the learning rate to 0.0002, and linearly decreased it to zero over the next 100 epochs. The size of patch was 56×56 and the size of mini-batch was 10. Kernels were initialized randomly from a Gaussian distribution. We have alternately updated the generator and the discriminator at each epoch. We normalized the intensity of the input low-dose CT images and the target routine-dose CT image using the maximum intensity value of the input images, and subtract 0.5 and multiply two to make the input image intensity range as $[-1, 1]$. For training, we used 50 cases from the dataset of mitral valve prolapse patients. The proposed method was implemented in Python with the PyTorch [29] and NVIDIA GeForce GTX 1080 Ti GPU was used to train and test the network.

C. Evaluation

1) *Visual grading analysis*: Qualitative image quality was assessed using relative visual grading analysis (VGA). This VGA method is planned to be related to the clinical task to evaluate any structural abnormality that may present at specific anatomical structures in a CT images. Two expert cardiac radiologists established a set of anatomical structures to evaluate image quality. Table I demonstrates the 13 anatomical structures used in this study. The VGA scoring scale are shown in Table II. All CT images including denoising CT images were uploaded on picture archiving and communication system (PACS) for visual grading. Of all, randomly selected 25 CT scans from mitral valve prolapse patients and 25 CT scans from coronary artery disease patients were included for VGA. Total 1300 CT images (50 selected CT scans \times 13 structures \times original and denoising CT) were scored. Two radiologists performed VGA in consensus, and all CT scans are scored independently, without side-by-side comparison.

2) *Quantitative analysis*: The image noise and signal-to-noise (SNR) of all images were obtained at four anatomical structures: ascending aorta, left ventricular cavity, left

TABLE II

VISUAL GRADING ANALYSIS SCORES USED TO EVALUATE THE STRUCTURE VISIBILITY

Score	Visibility of the structures in relation to the reference images
1	Poor image quality
2	Lower image quality
3	Mild noise, but acceptable
4	Average
5	Good
6	Excellent

ventricular septum, and proximal right coronary artery. The size of region of interest to evaluate SNR were varied to fit each anatomic structure; however, it was confined into each structure without overlapping other structures.

D. Statistical analysis

VGA scores obtained from original CT images and denoising images were compared using chi-square test. Image noise and SNR were compared using paired *t*-test. *P*-values of < 0.05 indicated statistical significance. Statistical analyses were performed using commercial software (SPSS, Chicago, IL, United States).

IV. RESULTS

A. Qualitative evaluation

To verify the performance of the proposed method, we tested 50 cases from the dataset of mitral valve prolapse patients which were not used in the training session. Also, we tested 50 cases from the dataset coronary artery disease patients which were not used to training the network. The results are described in Fig. 5 and 6, respectively. Each row indicates the different patient case, and the restoration results from the first column are shown in the second column. The input low-dose CT images are from phase 1 and the target routine-dose images are from phase 8. Due to the cardiac motion during CT scanning, the shape of the heart and image intensity from the contrast agent are different at the two phases. Distinct differences are indicated by the yellow arrows in the images. The denoised results showed that the proposed method is good at reducing the noise in the input CT images while the texture information and edges are still intact. The difference images showed that the proposed method did not change the detailed information and only removes noise from the input CT images.

We found that the proposed method is robust to the type of input CT images and the existence of contrast agent. Also, it is robust to the type of heart disease as confirmed in another disease cases in Fig. 6. Results showed that the network does not create any artificial features that can disturb the diagnosis while maintaining the crucial information.

We also observed that the proposed method is automatically adapted to the noise levels of the input CT images. Specifically, there are some data which have similar noise level between phase 1 and phase 8 as shown in Fig. 7. When the input CT

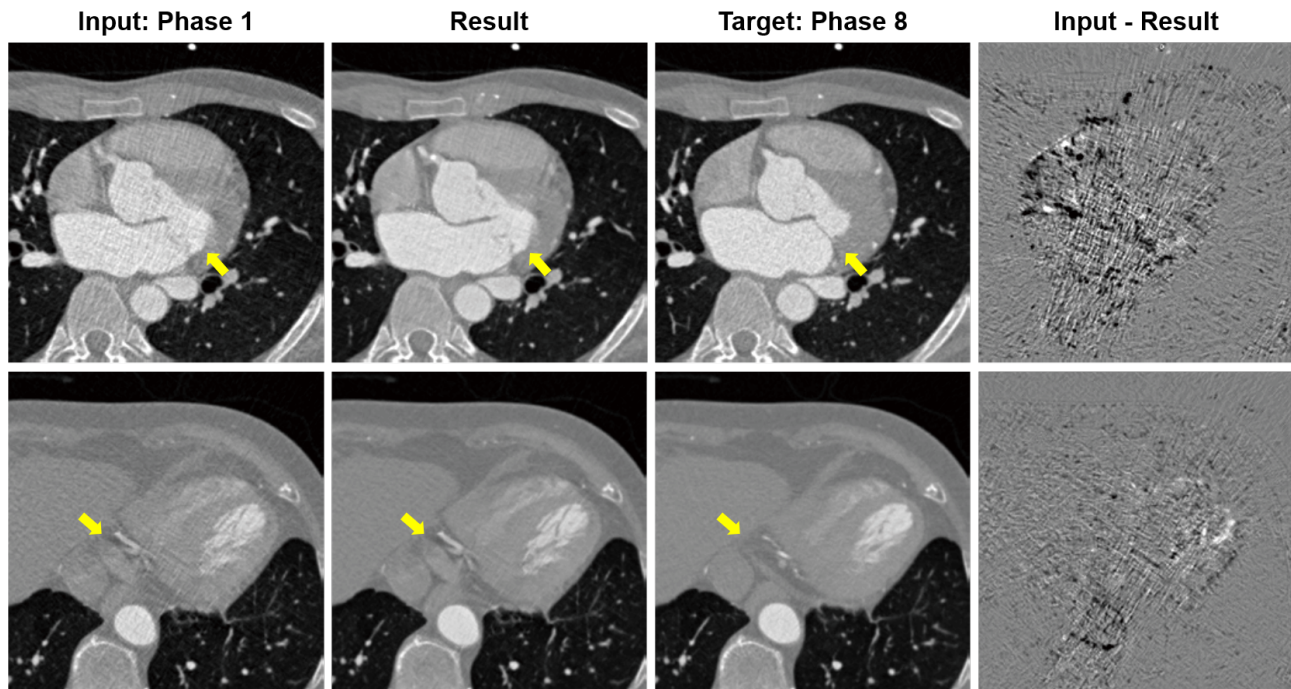


Fig. 5. Restoration results from the dataset of mitral valve prolapse patients. Intensity range of the CT image is $(-1024, 976)$ [HU] and the difference image between the input and result is $(-150, 150)$ [HU]. Yellow arrow indicates the distinctly different region between input image from phase 1 and target image from phase 8.

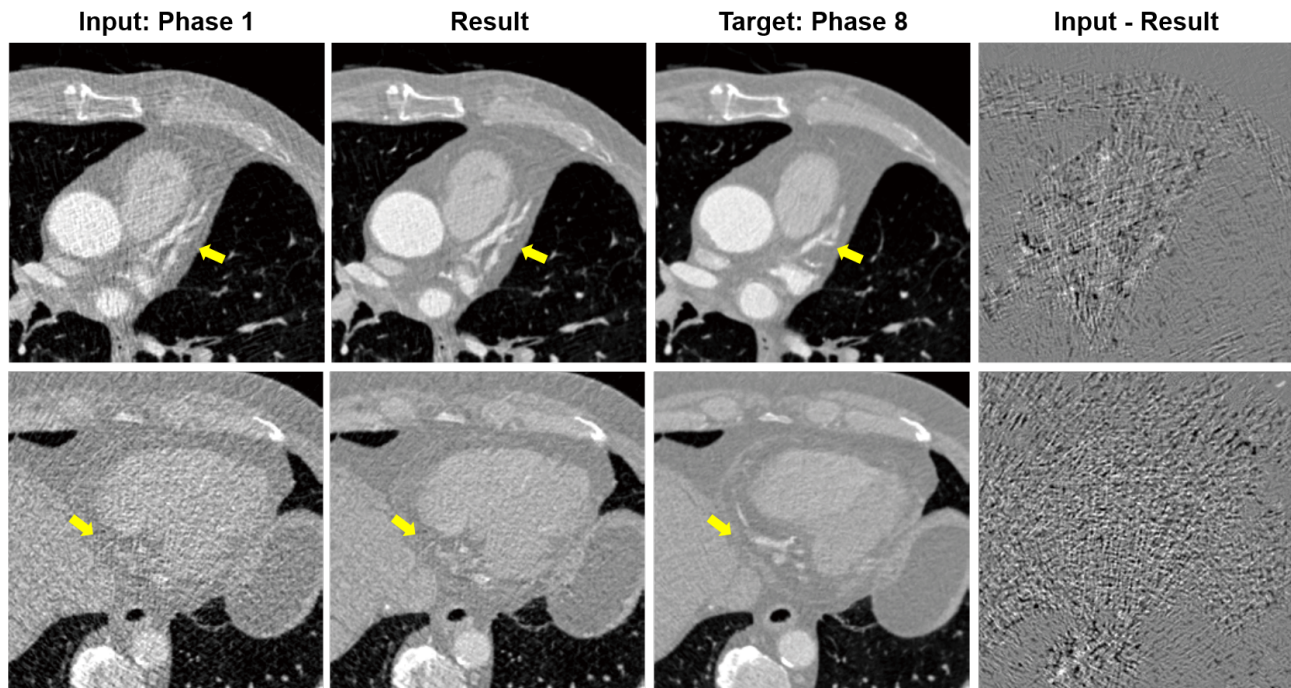


Fig. 6. Restoration results from the dataset of coronary artery disease patients. Intensity range of the CT image is $(-924, 576)$ [HU] and the difference image between the input and result is $(-200, 200)$ [HU]. Yellow arrow indicates the distinctly different region between input image from phase 1 and target image from phase 8.

images have similar noise level with the target CT images, we found that the proposed generator G_{AB} did not make any change as illustrated in Fig. 7. These results confirm the proposed generator G_{AB} satisfies the identity condition in (6) to only remove noises. These results ensure that the proposed

network does not generate artificial features.

B. Visual grading score and SNR analysis results

All visual scores are significantly higher in denoising CT, representing that the image quality of denoising CT is better

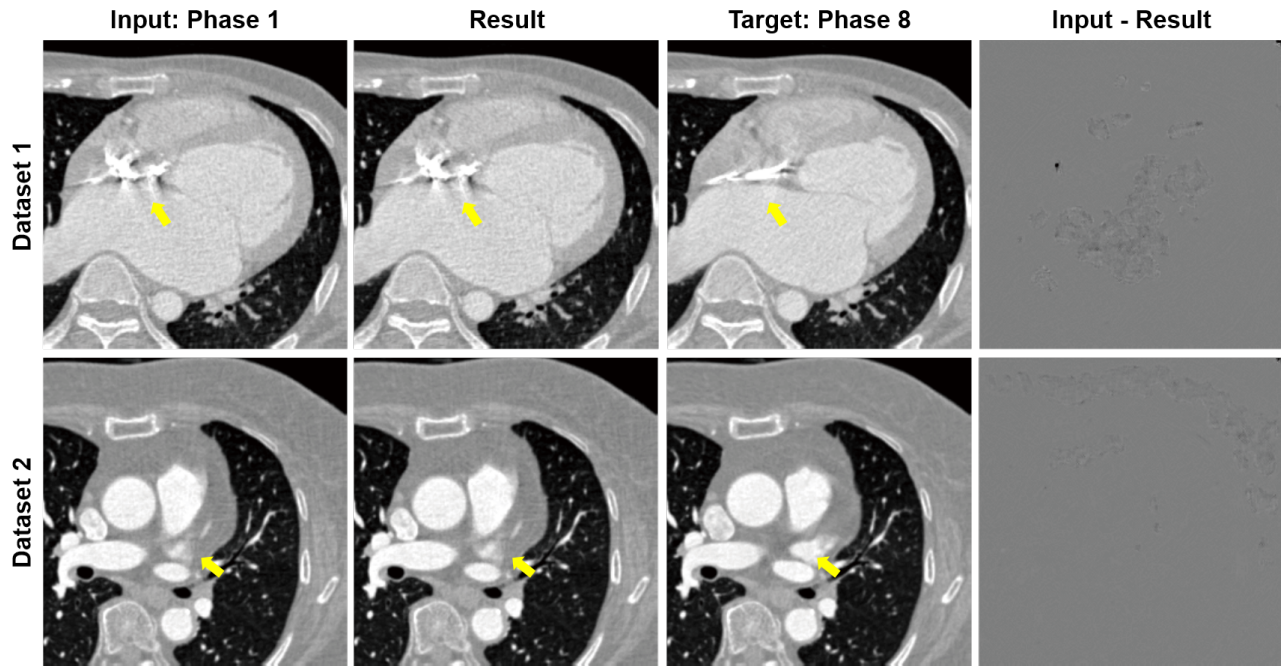


Fig. 7. Restoration results from the dataset whose input CT images have similar noise level with the target CT images. Intensity range of the CT image is $(-924, 576)$ [HU] and the difference image between the input and result is $(-15, 15)$ [HU]. Yellow arrow indicates the distinct different region between input image from phase 1 and target image from phase 8.

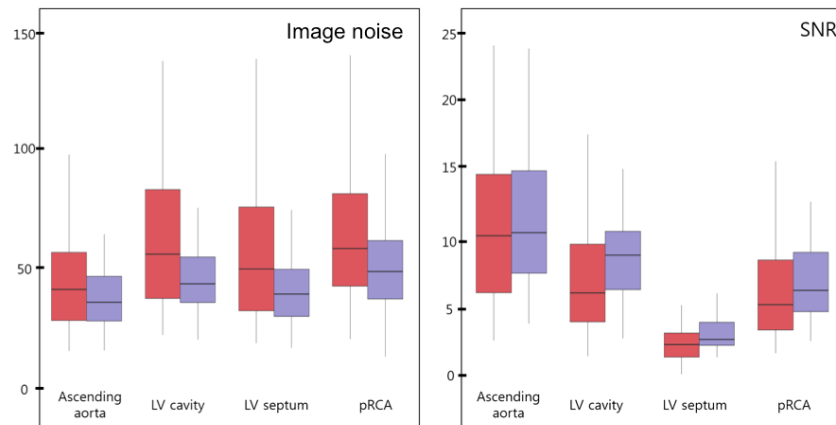


Fig. 8. Standard deviation and signal-to-noise ratio between original CT (red) and denoising CT (purple) images measured from selected structures. (LV, left ventricle; pRCA, proximal right coronary artery)

($P < 0.001$) (Table III). Quantitatively, image noise was decreased, and SNR was significantly increased on denoising CT ($P < 0.05$) (Table IV, Fig. 8), except no statistically significant SNR changes detected in left ventricular cavity where contrast enhanced blood pool measured by the largest region of interest ($P = 0.96$).

V. DISCUSSION

A. Ablation study

To demonstrate the optimality of the proposed network architecture, we performed ablation studies by excluding the identity loss and/or cyclic loss, and applying the same training procedures. The results with respect to two different noise

levels are illustrated in Fig. 9 and Fig. 10, respectively. Recall that the input low-dose CT image in the sub-figure (a) and target routine-dose image in the sub-figure (e) have different shape of heart due to the cardiac motion. The results of the proposed method are illustrated in the second column, the results of the excluding the identity loss are in the third column, and the results of the excluding the identity loss and cyclic loss are illustrated in the fourth column. We illustrate reconstruction images as well as the difference images between the input and the reconstruction results. We also indicate the artificial features that were not present in the input images by red arrows.

All the reconstruction result images in Fig. 9 show that

TABLE III
COMPARISON OF VISUAL SCORES BETWEEN ORIGINAL IMAGE AND DENOISING CT IMAGE USING CHI SQUARE METHOD. (LCA, LEFT CORONARY ARTERY; LV, LEFT VENTRICLE; RCA, RIGHT CORONARY ARTERY; RV, RIGHT VENTRICLE)

Organ	Structure	Original image	Denoising	P-value
Left/right coronary artery	LCA ostium	3.5 ± 1.4	4.2 ± 1.1	< 0.001
	LCA distal 1.5 cm	3.4 ± 1.4	4.1 ± 1.1	< 0.001
	LCA distal	2.3 ± 1.3	3.0 ± 1.2	< 0.001
	RCA ostium	3.3 ± 1.3	4.0 ± 1.0	< 0.001
	RCA 1.5 cm	3.1 ± 1.6	3.9 ± 1.1	< 0.001
	RCA distal	2.3 ± 1.4	2.8 ± 1.2	< 0.001
Cardiac wall	LV septum	3.1 ± 1.6	3.8 ± 1.2	< 0.001
	RV free wall margin	3.2 ± 1.4	3.8 ± 1.1	< 0.001
Cardiac cavity	LV trabeculation	3.4 ± 1.5	4.3 ± 1.1	< 0.001
	Left arterial appendage	3.0 ± 1.4	3.6 ± 0.9	< 0.001
Aorta	Aortic root	4.3 ± 1.2	5.0 ± 0.5	< 0.001
Valve	Aortic valve	2.8 ± 1.4	3.4 ± 0.9	< 0.001
	Mitral valve	2.8 ± 1.4	3.4 ± 1.0	< 0.001

TABLE IV
COMPARISON OF STANDARD DEVIATION AND SIGNAL-TO-NOISE RATIO BETWEEN ORIGINAL CT AND DENOISING CT IMAGES MEASURED FROM SELECTED STRUCTURES (LV, LEFT VENTRICLE; PRCA, PROXIMAL RIGHT CORONARY ARTERY;)

	Image noise (standard deviation)		P-value	SNR		P-value
	Original image	Denoising		Original image	Denoising	
Ascending aorta	48.0 ± 26.8	39.0 ± 17.0	0.003	11.1 ± 6.5	12.3 ± 6.2	0.001
LV cavity	69.4 ± 37.9	48.5 ± 19.0	< 0.001	8.9 ± 12.7	9.0 ± 3.5	0.96
LV septum	63.2 ± 40.8	40.9 ± 14.0	< 0.001	2.9 ± 1.7	3.4 ± 1.3	0.015
pRCA	70.5 ± 50.7	62.1 ± 48.5	0.036	6.4 ± 3.9	7.6 ± 4.4	0.034

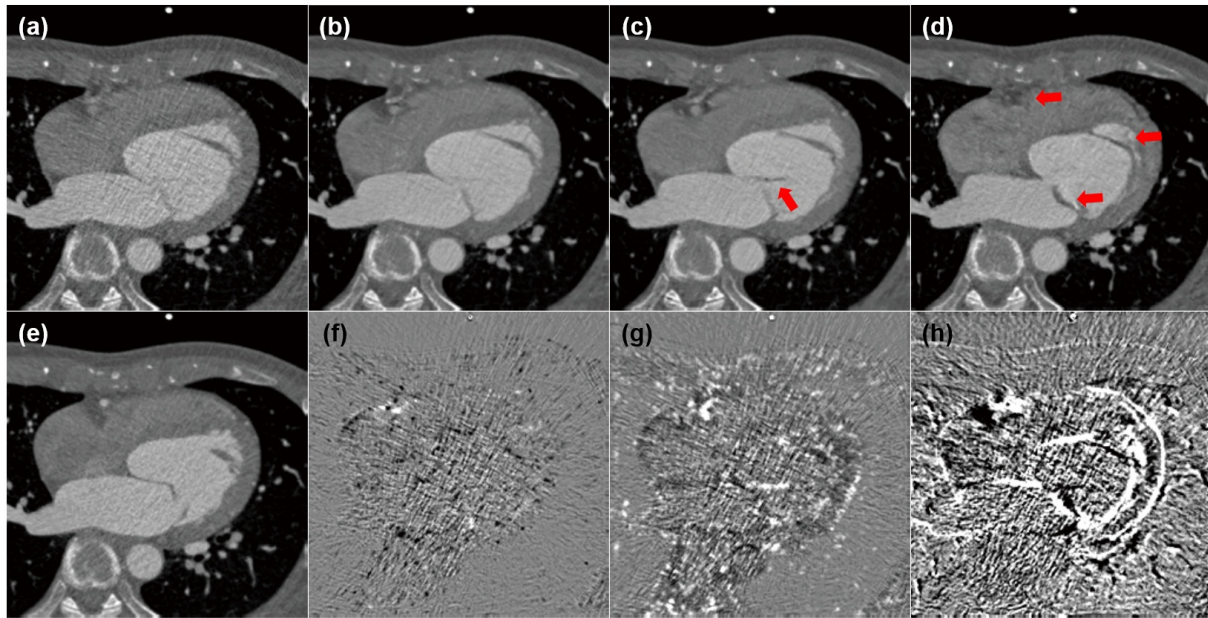


Fig. 9. (a) Input CT image, (b) proposed method, (c) proposed method without identity loss, (d) with only GAN loss, (e) target CT image, (f-h) difference images between input image and result images (b-d), respectively. Intensity range of the CT image is (-820, 1430)[HU] and the difference image between the input and result is (-200, 200)[HU]. Red arrow indicates the artificial features that were not present in the input image.

the noise level is reduced and the edge information is well maintained. However, while the proposed method does not generate any artificial features, the other methods generated some structures which are not present in the input images. The result of the excluding the identity loss (third column) are better than the network trained only with GAN loss without

including cycle consistency and identity loss (fourth column), but both methods deformed the shape of the heart and removed some structures. Similar observations can be found in Fig. 10 where input CT image has a similar noise level with target CT image. While the proposed method maintains the original images, the other methods deformed the shape and

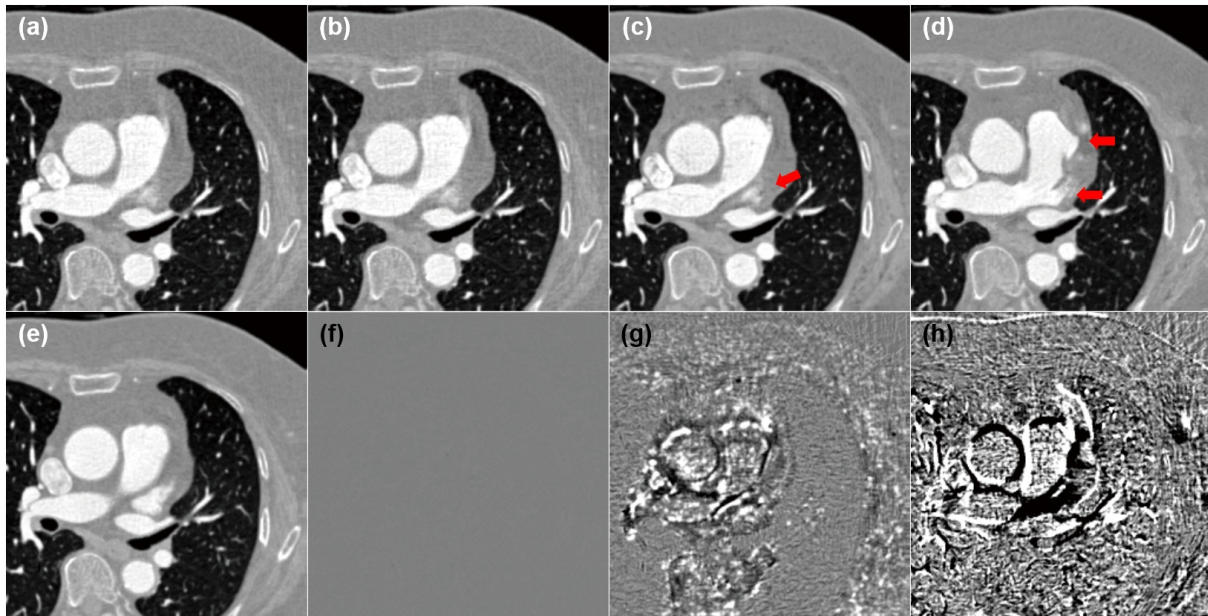


Fig. 10. (a) Input CT image, (b) proposed method, (c) proposed method without identity loss, (d) with only GAN loss, (e) target CT image, (f-h) difference images between input image and result images (b-d), respectively. Intensity range of the CT image is $(-924, 576)$ [HU] and the difference image between the input and result is $(-100, 100)$ [HU]. Red arrow indicates the artificial features that were not present in the input image.

generates the features that were not present in the input image. Considering that artificial features can confuse the radiologists in diagnosing the patient's disease, the result confirmed the critical importance of the cyclic loss and identity loss as proposed in our algorithm.

VI. CONCLUSION

In this paper, we proposed a cycle consistent adversarial denoising network for multiphase coronary CT angiography. Unlike the existing supervised deep learning approaches for low-dose CT, our network does not require exactly matched low- and routine- dose images. Instead, our network was designed to learn the image distributions from the high-dose cardiac phases. Furthermore, in contrast to the other state-of-the-art deep neural networks with GAN loss that are prone to generate artificial features, our network was designed to prevent from generating artificial features that are not present in the input image by exploiting the cyclic consistency and identity loss. Experimental results confirmed that the proposed method is good at reducing the noise in the input low-dose CT images while retain the texture and edge information. Moreover, when the routine dose images were used as input, the proposed network did not change the images, confirming that the algorithm correctly learn the noises. Radiological evaluation using visual grading analysis scores also confirmed that the proposed denoising method significantly increases the diagnostic quality of the images.

Considering the effectiveness and practicability of the proposed method, we believe that the proposed method can be widely applied for other CT acquisition protocols with dynamic tube current modulation.

ACKNOWLEDGEMENT

This work is supported by Industrial Strategic technology development program (10072064, Development of Novel Artificial Intelligence Technologies To Assist Imaging Diagnosis of Pulmonary, Hepatic, and Cardiac Disease and Their Integration into Commercial Clinical PACS Platforms) funded by the Ministry of Trade Industry and Energy (MI, Korea).

REFERENCES

- [1] J. Hsieh, *Computed tomography: principles, design, artifacts, and recent advances*. SPIE, Bellingham, WA, 2009.
- [2] M. Beister, D. Kolditz, and W. A. Kalender, "Iterative reconstruction methods in X-ray CT," *Physica Medica*, vol. 28, no. 2, pp. 94–108, 2012.
- [3] S. Ramani and J. A. Fessler, "A splitting-based iterative algorithm for accelerated statistical X-ray CT reconstruction," *IEEE Transactions on Medical Imaging*, vol. 31, no. 3, pp. 677–688, 2012.
- [4] E. Y. Sidky and X. Pan, "Image reconstruction in circular cone-beam computed tomography by constrained, total-variation minimization," *Physics in Medicine and Biology*, vol. 53, no. 17, pp. 4777–4807, 2008.
- [5] J. Leipsic, T. M. LaBounty, B. Heilbron, J. K. Min, G. J. Mancini, F. Y. Lin, C. Taylor, A. Dunning, and J. P. Earls, "Adaptive statistical iterative reconstruction: assessment of image noise and image quality in coronary CT angiography," *American Journal of Roentgenology*, vol. 195, no. 3, pp. 649–654, 2010.
- [6] Y. Funama, K. Taguchi, D. Utsunomiya, S. Oda, Y. Yanaga, Y. Yamashita, and K. Awai, "Combination of a low tube voltage technique with the hybrid iterative reconstruction (iDose) algorithm at coronary CT angiography," *Journal of computer assisted tomography*, vol. 35, no. 4, p. 480, 2011.
- [7] G.-H. Chen, J. Tang, and S. Leng, "Prior image constrained compressed sensing (PICCS): a method to accurately reconstruct dynamic CT images from highly undersampled projection data sets," *Medical physics*, vol. 35, no. 2, pp. 660–663, 2008.
- [8] M. Renker, J. W. Nance Jr, U. J. Schoepf, T. X. O'Brien, P. L. Zwerner, M. Meyer, J. M. Kerl, R. W. Bauer, C. Fink, T. J. Vogl *et al.*, "Evaluation of heavily calcified vessels with coronary CT angiography: comparison of iterative and filtered back projection image reconstruction," *Radiology*, vol. 260, no. 2, pp. 390–399, 2011.

- [9] E. Kang, J. Min, and J. C. Ye, "A deep convolutional neural network using directional wavelets for low-dose X-ray CT reconstruction," *Medical Physics*, vol. 44, no. 10, 2017.
- [10] E. Kang, W. Chang, J. Yoo, and J. C. Ye, "Deep convolutional framelet denoising for low-dose CT via wavelet residual network," *IEEE transactions on medical imaging*, vol. 37, no. 6, pp. 1358–1369, 2018.
- [11] H. Chen, Y. Zhang, M. K. Kalra, F. Lin, Y. Chen, P. Liao, J. Zhou, and G. Wang, "Low-dose CT with a residual encoder-decoder convolutional neural network," *IEEE Transactions on Medical Imaging*, vol. 36, no. 12, pp. 2524–2535, 2017.
- [12] Q. Yang, P. Yan, Y. Zhang, H. Yu, Y. Shi, X. Mou, M. K. Kalra, Y. Zhang, L. Sun, and G. Wang, "Low dose CT image denoising using a generative adversarial network with Wasserstein distance and perceptual loss," *IEEE Transactions on Medical Imaging*, vol. 37, no. 6, pp. 1348 – 1357, 2018.
- [13] J. C. Ye, Y. Han, and E. Cha, "Deep convolutional framelets: A general deep learning framework for inverse problems," *SIAM Journal on Imaging Sciences*, vol. 11, no. 2, pp. 991–1048, 2018.
- [14] Y. Han and J. C. Ye, "Framing u-net via deep convolutional framelets: Application to sparse-view CT," *IEEE Transactions on Medical Imaging*, vol. 37, no. 6, pp. 1418–1429, 2018.
- [15] K. H. Jin, M. T. McCann, E. Froustey, and M. Unser, "Deep convolutional neural network for inverse problems in imaging," *IEEE Transactions on Image Processing*, vol. 26, no. 9, pp. 4509–4522, 2017.
- [16] J. Adler and O. Öktem, "Learned primal-dual reconstruction," *IEEE Transactions on Medical Imaging*, vol. 37, no. 6, pp. 1322–1332, 2018.
- [17] J. M. Wolterink, T. Leiner, M. A. Viergever, and I. Isgum, "Generative adversarial networks for noise reduction in low-dose CT," *IEEE Transactions on Medical Imaging*, pp. 2536–2545, 2017.
- [18] Q. Yang, P. Yan, Y. Zhang, H. Yu, Y. Shi, X. Mou, M. K. Kalra, and G. Wang, "Low dose CT image denoising using a generative adversarial network with Wasserstein distance and perceptual loss," *IEEE Transactions on Medical Imaging*, 2018.
- [19] X. Yi and P. Babyn, "Sharpness-aware low-dose ct denoising using conditional generative adversarial network," *Journal of Digital Imaging*, Feb 2018.
- [20] J.-Y. Zhu, T. Park, P. Isola, and A. A. Efros, "Unpaired image-to-image translation using cycle-consistent adversarial networks," in *2017 IEEE International Conference on Computer Vision (ICCV)*. IEEE, 2017, pp. 2242–2251.
- [21] T. Kim, M. Cha, H. Kim, J. K. Lee, and J. Kim, "Learning to discover cross-domain relations with generative adversarial networks," in *International Conference on Machine Learning*, 2017, pp. 1857–1865.
- [22] I. Goodfellow, J. Pouget-Abadie, M. Mirza, B. Xu, D. Warde-Farley, S. Ozair, A. Courville, and Y. Bengio, "Generative adversarial nets," in *Advances in Neural Information Processing Systems 27*, Z. Ghahramani, M. Welling, C. Cortes, N. D. Lawrence, and K. Q. Weinberger, Eds. Curran Associates, Inc., 2014, pp. 2672–2680.
- [23] X. Mao, Q. Li, H. Xie, R. Y. Lau, Z. Wang, and S. P. Smolley, "Least squares generative adversarial networks," in *2017 IEEE International Conference on Computer Vision (ICCV)*. IEEE, 2017, pp. 2813–2821.
- [24] P. Isola, J.-Y. Zhu, T. Zhou, and A. A. Efros, "Image-to-image translation with conditional adversarial networks," in *2017 IEEE Conference on Computer Vision and Pattern Recognition (CVPR)*, 2017.
- [25] K. He, X. Zhang, S. Ren, and J. Sun, "Deep residual learning for image recognition," in *2016 IEEE Conference on Computer Vision and Pattern Recognition (CVPR)*, 2016, pp. 770–778.
- [26] H. J. Koo, D. H. Yang, S. Y. Oh, J.-W. Kang, D.-H. Kim, J.-K. Song, J. W. Lee, C. H. Chung, and T.-H. Lim, "Demonstration of mitral valve prolapse with ct for planning of mitral valve repair," *RadioGraphics*, vol. 34, no. 6, pp. 1537–1552, 2014.
- [27] D. H. Yang, Y.-H. Kim, J.-H. Roh, J.-W. Kang, D. Han, J. Jung, N. Kim, J. B. Lee, J.-M. Ahn, J.-Y. Lee, D.-W. Park, S.-J. Kang, S.-W. Lee, C. W. Lee, S.-W. Park, S.-J. Park, and T.-H. Lim, "Stress myocardial perfusion ct in patients suspected of having coronary artery disease: Visual and quantitative analysisvalidation by using fractional flow reserve," *Radiology*, vol. 276, no. 3, pp. 715–723, 2015.
- [28] A. C. Weustink, N. R. Mollet, F. Pugliese, W. B. Meijboom, K. Nieman, M. H. Heijnenbrok-Kal, T. G. Flohr, L. A. E. Neeffjes, F. Cademartiri, P. J. de Feyter, and G. P. Krestin, "Optimal electrocardiographic pulsing windows and heart rate: Effect on image quality and radiation exposure at dual-source coronary ct angiography," *Radiology*, vol. 248, no. 3, pp. 792–798, 2008.
- [29] A. Paszke, S. Gross, S. Chintala, G. Chanan, E. Yang, Z. DeVito, Z. Lin, A. Desmaison, L. Antiga, and A. Lerer, "Automatic differentiation in pytorch," in *NIPS-W*, 2017.